

A Geometric Interpretation of Southern Ocean Eddy Form Stress

MADS B. POULSEN AND MARKUS JOCHUM

Niels Bohr Institute, University of Copenhagen, Copenhagen, Denmark

JAMES R. MADDISON

School of Mathematics, and Maxwell Institute for Mathematical Sciences, University of Edinburgh, Edinburgh, United Kingdom

DAVID P. MARSHALL

Department of Physics, University of Oxford, Oxford, United Kingdom

ROMAN NUTERMAN

Niels Bohr Institute, University of Copenhagen, Copenhagen, Denmark

(Manuscript received 26 October 2018, in final form 20 July 2019)


ABSTRACT

An interpretation of eddy form stress via the geometry described by the Eliassen–Palm flux tensor is explored. Complementary to previous works on eddy Reynolds stress geometry, this study shows that eddy form stress is fully described by a vertical ellipse, whose size, shape, and orientation with respect to the mean flow shear determine the strength and direction of vertical momentum transfers. Following a recent proposal, this geometric framework is here used to form a Gent–McWilliams eddy transfer coefficient that depends on eddy energy and a nondimensional geometric parameter α , bounded in magnitude by unity. The parameter α expresses the efficiency by which eddies exchange energy with baroclinic mean flow via along-gradient eddy buoyancy flux—a flux equivalent to eddy form stress along mean buoyancy contours. An eddy-resolving ocean general circulation model is used to estimate the spatial structure of α in the Southern Ocean and assess its potential to form a basis for parameterization. The eddy efficiency α averages to a low but positive value of 0.043 within the Antarctic Circumpolar Current, consistent with an inefficient eddy field extracting energy from the mean flow. It is found that the low eddy efficiency is mainly the result of that eddy buoyancy fluxes are weakly anisotropic on average. The eddy efficiency is subject to pronounced vertical structure and is maximum at ~ 3 -km depth, where eddy buoyancy fluxes tend to be directed most downgradient. Since α partly sets the eddy form stress in the Southern Ocean, a parameterization for α must reproduce its vertical structure to provide a faithful representation of vertical stress divergence and eddy forcing.

1. Introduction

The Antarctic Circumpolar Current is embedded in a rich mesoscale eddy field, as readily seen from both satellite altimetry and realistic eddy-resolving model simulations (Storch et al. 2012; Roulet et al. 2014; Frenger et al. 2015; Stewart et al. 2015). The vertical

structure of the eddy field is associated with undulated interior ocean neutral surfaces which enable a vertical transfer of horizontal momentum through eddy form stress (Johnson and Bryden 1989; Wolff et al. 1991; Ivchenko et al. 1996; Olbers 1998). This process is fundamental to the dynamics of the Southern Ocean as it causes a net downward momentum transfer which permits a governing momentum balance between surface wind stress and topographic form drag across

 Denotes content that is immediately available upon publication as open access.

Corresponding author: Mads Bruun Poulsen, mads.poulsen@nbi.ku.dk



This article is licensed under a Creative Commons Attribution 4.0 license (<http://creativecommons.org/licenses/by/4.0/>).

DOI: 10.1175/JPO-D-18-0220.1

© 2019 American Meteorological Society

shallow ridges and continents (Munk and Palmén 1951; Masich et al. 2015). For adiabatic and geostrophic eddies the zonal eddy form stress additionally induces a meridional circulation that compensates Southern Ocean wind-driven overturning (Danabasoglu et al. 1994; Marshall 1997; Marshall and Radko 2003; Viebahn and Eden 2010), with implication for the strength and structure of the residual circulation.

Recent studies have highlighted that eddy form stress is predominantly localized in several standing meanders within the circumpolar current (Thompson and Garabato 2014; Masich et al. 2018). This zonal heterogeneity has also been reported in the upwelling associated with the residual overturning circulation (Tamsitt et al. 2017). The meanders form when large-scale flow navigates submarine topographic obstacles and are associated with elevated deep-reaching eddy kinetic energy (Hallberg and Gnanadesikan 2001; Bischoff and Thompson 2014; Barthel et al. 2017). In addition both eddy-resolving models and observations show that the transport of the Antarctic Circumpolar Current is insensitive to a strengthening of the zonal wind stress (Hallberg and Gnanadesikan 2006; Meredith and Hogg 2006; Böning et al. 2008; Munday et al. 2013; Morrison and Hogg 2013; Marshall et al. 2017; Poulsen et al. 2018). This is thought to be the consequence of a concurrent increase of eddy form stress which is able to balance the additional surface momentum flux, a phenomenon known as eddy saturation (Straub 1993).

The horizontal grid resolution of ocean general circulation models typically employed to study processes on centennial or millennial time scales does not permit explicit eddy form stress to develop. Instead the effects caused by the stress need to be introduced through parameterization, and the ability to represent Southern Ocean eddy form stress constitutes a key measure to assess the quality of any proposed eddy closure. Presently the most common approach is to use a skew-diffusive flux scheme with the diffusivity taken proportional to the isopycnal slope (Gent and McWilliams 1990; Griffies 1998). This choice ensures a removal of available potential energy from the large-scale flow, a fundamental property of baroclinic instability. The implementation of this scheme, however, requires a specification of an eddy transfer coefficient κ . Previous attempts to estimate κ based on inferred divergent eddy buoyancy fluxes find that it is a function of both time and space, and locally may be of negative sign (e.g., Roberts and Marshall 2000; Eden et al. 2007b). Different closures for the transfer coefficient as function of ocean stratification (Visbeck et al. 1997; Ferreira et al. 2005) or local eddy kinetic energy (Eden and Greatbatch 2008) have been

proposed, yet none of these has emerged as superior or able to support an eddy saturation regime (Eden et al. 2009; Farneti et al. 2015; Jochum and Eden 2015).

Marshall et al. (2012), in a quasigeostrophic context, introduces a framework in which eddy flux parameterization is based on the inherent geometric properties of the Eliassen–Palm flux tensor. This framework revolves around a decomposition of Reynolds and form stresses in terms of the total eddy energy and five bounded dimensionless parameters, related to the geometry of eddy fluxes of momentum and buoyancy. Provided with a prognostic equation for the eddy energy, the main hypothesis is that the bounds on the involved parameters render the eddy parameterization problem more tractable. A corollary that follows from their conceptual framework is a new expression for κ in terms of eddy energy E , oceanic stratification, and a dimensionless parameter α ,

$$\kappa = \alpha E \frac{\mathcal{N}_0}{\mathcal{M}^2}, \quad (1)$$

where \mathcal{N}_0 and \mathcal{M} refer to the local vertical and horizontal stratification, respectively. Parameter α , henceforth referred to as an eddy efficiency, carries information on the geometry of horizontal eddy buoyancy fluxes and is bounded by unity in magnitude. Results from implementation and analysis of Eq. (1) in idealized model setups, using a constant value for α , have shown promising representations of inferred tracer fluxes (Bachman et al. 2017) and eddy saturation (Mak et al. 2017, 2018).

Formally, the eddy geometry described in Marshall et al. (2012) is associated with two distinct ellipses; one in the horizontal plane related to eddy Reynolds stress, and one oriented in the vertical plane related to eddy form stress. The strength and anisotropy of the eddy stresses are expressed through the size and eccentricity of the ellipses, respectively, and the ellipse orientation with respect to the background velocity shear determines whether the eddies extract or surrender energy to the mean flow. In the case of eddy Reynolds stress, the energy transfer associated with the ellipse tilt is consistent with expectations from classical stability theory (Tamarin et al. 2016), and the geometric stress representation has previously been used to diagnose eddy–mean flow interactions in, for example, the atmospheric midlatitude westerlies (Hoskins et al. 1983), the Southern Ocean (Morrow et al. 1994), and in an idealized model of a western boundary current extension (Waterman and Hoskins 2013; Waterman and Lilly 2015). These studies, together with the attractive properties of the geometrically informed eddy transfer coefficient outlined in the preceding paragraph, suggest that a geometric

perspective is useful to understand and parameterize eddy–mean flow interactions.

While the application of the geometric framework to Reynolds stress is well documented in the literature, little attention has been dedicated to the eddy form stress geometry which is encapsulated in α . Marshall et al. (2012) examined the spatial structure of α in a quasigeostrophic model of a wind-driven gyre, demonstrating that its features relate to the large-scale circulation, but the structure of α in more complex settings is unknown. The most recent estimate for α is a spatially uniform value of 0.2, extracted from a highly idealized model of a baroclinically unstable current (Bachman et al. 2017).

The aim of the present study is twofold: first, to clarify the connection between the Eliassen–Palm flux tensor and its geometric interpretation in terms of two ellipses, and second, to diagnose the eddy form stress geometry in a global eddy-resolving general circulation. The latter objective is motivated by the desire to construct a parameterization for α for use in complex ocean models that employ Eq. (1). The analysis presented in this study is focused on the Southern Ocean where the vertical structure of eddy form stress is of primary importance to the momentum balance. The present work can be seen as complimentary to the study by Stewart et al. (2015) who examined the Reynolds stress anisotropy from both satellite altimetry and model output. Taken together these works are intended to provide guidance toward the long-term goal of a unified parameterization of eddy stresses via the Eliassen–Palm flux tensor.

The plan of the paper is the following. Section 2 reviews the stress decomposition by Marshall et al. (2012) and clarifies its geometric interpretation in terms of two distinct ellipses. Based on the eddy form stress decomposition, the eddy efficiency α is defined. Section 3 describes the setup of the numerical model and the simulation from which the eddy form stress geometry is computed. Section 4 presents and discusses the spatial structure of eddy buoyancy flux anisotropy, vertical eddy tilt, and horizontal orientation of eddy form stress, which all enter the expression for the eddy efficiency α . Discussion and a summary then follow in sections 5 and 6, respectively.

2. Geometric framework

a. Eddy stress tensor

The eddy forcing of the time-mean quasigeostrophic potential vorticity equation F_q is expressed through the divergence of the horizontal eddy potential vorticity

flux. This forcing is in turn related to the eddy stress tensor \mathbf{E} ,

$$F_q = \nabla_h \cdot [\mathbf{k} \times (\nabla \cdot \mathbf{E})], \quad (2)$$

where $-\nabla \cdot \mathbf{E}$ is the eddy forcing of the associated horizontal momentum equation. Here ∇ and ∇_h are the three-dimensional and horizontal divergence operator, respectively, and \mathbf{k} is the vertical unit vector. Equation (2) involves two applications of the divergence operator, hence certain gauge freedom is permitted in the specification of \mathbf{E} . As shown in Maddison and Marshall (2013) several natural choices for \mathbf{E} exist. The eddy stress tensor of interest in the present study is

$$\mathbf{E} = \begin{bmatrix} -M + 2K & N & 0 \\ N & M + 2K & 0 \\ -S & R & 0 \end{bmatrix}, \quad (3)$$

for reasons that are discussed below. Here M and N are the eddy Reynolds stresses,

$$M = \frac{\overline{v'_g v'_g} - \overline{u'_g u'_g}}{2}, \quad N = \overline{u'_g v'_g}, \quad (4)$$

R and S are the eddy form stresses,

$$R = \frac{f_0}{\mathcal{N}_0^2} \overline{b' u'_g}, \quad S = \frac{f_0}{\mathcal{N}_0^2} \overline{b' v'_g}, \quad (5)$$

and K is the eddy kinetic energy,

$$K = \frac{\overline{u'_g u'_g} + \overline{v'_g v'_g}}{2}. \quad (6)$$

The variables u'_g and v'_g are the horizontal geostrophic eddy velocities, f_0 is the reference Coriolis parameter, and the overline denotes an appropriate time mean. In accord with the quasigeostrophic approximation, the full buoyancy field is decomposed as $b_0(z) + b$ and the reference buoyancy frequency \mathcal{N}_0 is formulated with respect to the background buoyancy profile b_0 . The temporal buoyancy deviation b' is defined as $b' = b - \bar{b}$.

Marshall et al. (2012) derive energetic bounds for the magnitude of eddy Reynolds stress $M^2 + N^2$ and eddy form stress $R^2 + S^2$, which in combination bounds the norm of \mathbf{E} . The energetic bounds allow for an expression of the eddy stresses in terms of the eddy energy and five bounded dimensionless parameters related to the geometry of horizontal eddy fluxes of momentum and buoyancy. Following the discussion in Maddison and Marshall (2013), the decomposition of the constituents of \mathbf{E} is

$$\mathbf{M} = (M, N) = \gamma_m L \cos^2(\lambda^*) \mathbf{r}_m, \quad (7a)$$

$$\mathbf{R} = (R, S) = \gamma_b L \sin(2\lambda^*) \mathbf{r}_b, \quad (7b)$$

where

$$\mathbf{r}_m = [-\cos(2\phi_m), \sin(2\phi_m)], \quad (8a)$$

$$\mathbf{r}_b = [\cos(\phi_b), \sin(\phi_b)]. \quad (8b)$$

The quantity L is the sum of eddy kinetic energy and scaled eddy potential energy,

$$L = K + \frac{f_0^2}{\mathcal{N}_0^2} P = K + P^*, \quad (9)$$

where P is the quasigeostrophic eddy potential energy,

$$P = \frac{\overline{b'b'}}{2\mathcal{N}_0^2}. \quad (10)$$

The angle λ^* expresses the partitioning of L between potential and kinetic energy,

$$\frac{P^*}{L} = \sin^2(\lambda^*), \quad \frac{K}{L} = \cos^2(\lambda^*), \quad (11)$$

and is bounded between 0 and $\pi/2$.

The goal of the following subsections is to clarify the physical interpretation of the geometric parameters ϕ_m , γ_m , ϕ_b and γ_b . The main tool to achieve this goal is quadratic forms, $\mathbf{x}^T \mathbf{B} \mathbf{x} = 1$, where \mathbf{B} is any rank-two tensor, \mathbf{x} is a displacement vector, and the superscript T denotes the transpose. A quadratic form describes a geometric object; the eigenvectors of \mathbf{B} lie along the principal axes of the geometric object, and the eigenvalues are equal to the squared radii along the principal axes and hence determine the object shape (Riley et al. 2006). Prior to analysis of the geometric object described by \mathbf{E} , it is useful to consider a division of \mathbf{E} into two contributions,

$$\mathbf{E} = \mathbf{E}_m + \mathbf{E}_b. \quad (12)$$

In the present study, this division consists of

$$\mathbf{E}_m = \begin{bmatrix} -M + K & N & 0 \\ N & M + K & 0 \\ 0 & 0 & -P^* \end{bmatrix}, \quad (13)$$

which is termed the eddy Reynolds stress tensor, and

$$\mathbf{E}_b = \begin{bmatrix} K & 0 & 0 \\ 0 & K & 0 \\ -S & R & P^* \end{bmatrix}, \quad (14)$$

which is termed the eddy form stress tensor. Since $\mathbf{x}^T \mathbf{A} \mathbf{x} = 0$ for any antisymmetric tensor \mathbf{A} , the matrix representation of quadratic forms is nonunique and the geometry described by any \mathbf{B} is associated with its symmetric part, $(\mathbf{B} + \mathbf{B}^T)/2$, only. For the eddy form stress tensor \mathbf{E}_b , the symmetric contribution is

$$\frac{1}{2}(\mathbf{E}_b + \mathbf{E}_b^T) = \begin{bmatrix} K & 0 & -S/2 \\ 0 & K & R/2 \\ -S/2 & R/2 & P^* \end{bmatrix}. \quad (15)$$

The particular form of \mathbf{E} , Eq. (3), and its division into \mathbf{E}_m and \mathbf{E}_b , is not unique, but is motivated by the following:

- The tensor division permits an examination of Reynolds and form stress geometry individually.
- In the absence of buoyancy fluctuations, \mathbf{E}_m is identical to the eddy stress tensor discussed in Waterman and Lilly (2015) for barotropic systems and the eddy forcing is completely described by \mathbf{E}_m .
- Both \mathbf{E}_m and \mathbf{E}_b resemble covariance tensors, with variances on the diagonal and covariances on the off-diagonal. This tensor form implies that it is possible to relate \mathbf{E} to the geometry of variance ellipses, or its higher dimensional form, which are commonly used to visualize multivariate statistics.

The last point is of particular interest as the connection between eddy forcing and variance ellipse geometry has been established in Waterman and Lilly (2015). The geometric objects described by \mathbf{E}_m and \mathbf{E}_b , and their relation to variance ellipses, are the foci of the following subsections.

b. Eddy Reynolds stress ellipse

The eddy Reynolds stress tensor \mathbf{E}_m has eigenvalues $-P^*$ and

$$\Lambda_{\pm} = K(1 \pm \gamma_m), \quad (16)$$

where

$$\gamma_m = \frac{\Lambda_+ - \Lambda_-}{\Lambda_+ + \Lambda_-} = \sqrt{\frac{M^2 + N^2}{K^2}} \quad (17)$$

is the eddy momentum flux anisotropy, which in Marshall et al. (2012) is shown to be bounded between zero and unity, $0 \leq \gamma_m \leq 1$. According to the sign of the eigenvalues, \mathbf{E}_m describes a hyperboloid. The momentum covariances N are the only nonzero off-diagonal terms in \mathbf{E}_m and suggest that a horizontal section of the hyperboloid results in a more concise representation of the relevant eddy Reynolds stress geometry. Specifically, if

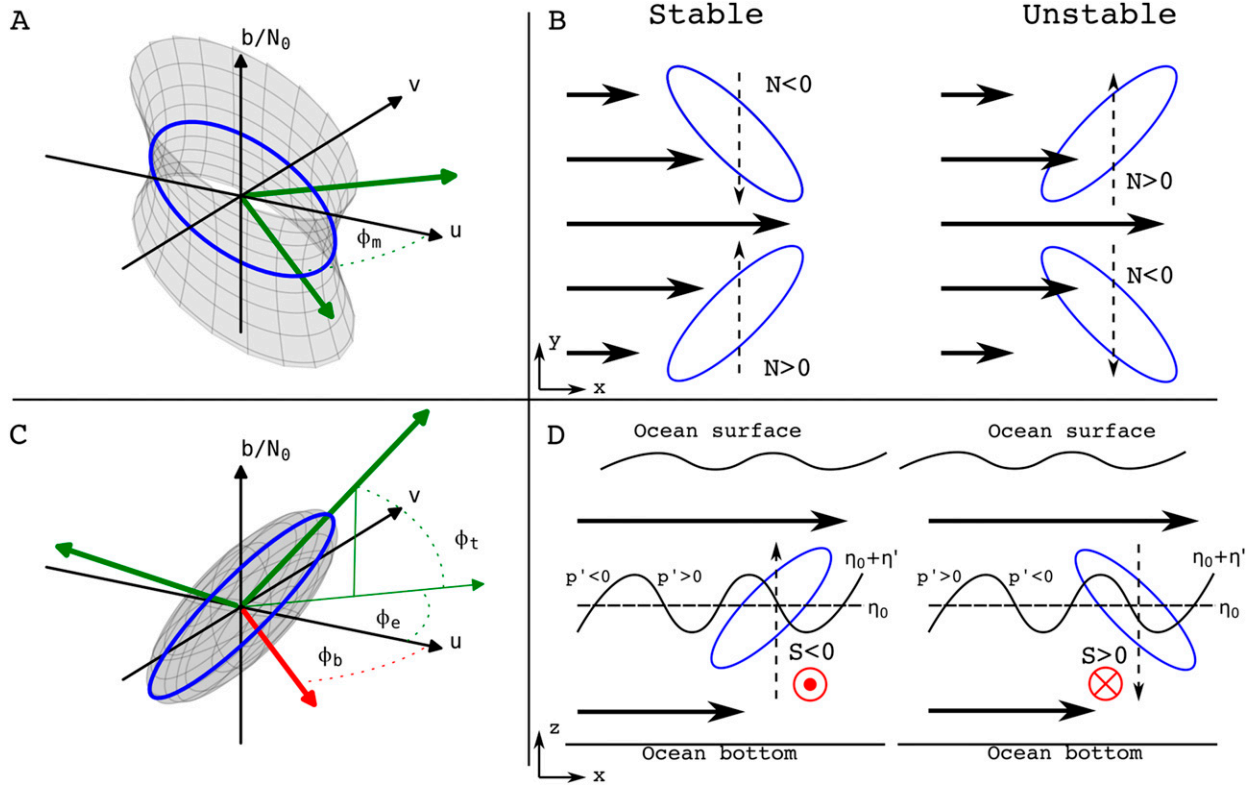


FIG. 1. (a) Horizontal ellipse (blue) and principal axes (green eigenvectors) described by the eddy Reynolds stress tensor, Eq. (18). The angle ϕ_m provides the orientation of the major axis with respect to the zonal direction. The Reynolds stress ellipse is formally the cross section between a horizontal plane and the hyperboloid (black mesh) described by Eq. (13). (b) Eddy-mean flow interaction in horizontally sheared mean flow (black solid arrows) as diagnosed with the use of the Reynolds stress ellipse. The shear sharpens when the ellipse leans with the shear ($\partial N/\partial y < 0$) and weakens when the ellipse leans into the shear ($\partial N/\partial y > 0$). The dashed black arrows show the direction of the zonal momentum transfer. (c) Vertical ellipse (blue) and principal axes (thick green eigenvectors) described by the eddy form stress tensor, Eq. (26). The red arrow is the horizontal (R, S) vector, which is perpendicular to the ellipse major axis, $\phi_e = \phi_b + \pi/2$. The ellipse is formally the cross section between a vertical plane and the ellipsoid (black mesh) described by Eq. (14). (d) Eddy-mean flow interaction in vertically sheared zonal mean flow (black solid arrows) as diagnosed with the use of the form stress ellipse. When $\overline{\eta' \partial p' / \partial x} < 0$, $S > 0$, the ellipse leans into the shear and the momentum transfer (black dashed arrows) is downward, which acts to weaken the shear. The opposite is the case when the ellipse leans with the shear.

\mathbf{T}_h is the transformation matrix that consists of the two basis vectors in \mathbb{R}^3 that span the horizontal plane, a transformation of \mathbf{E}_m using \mathbf{T}_h results in

$$\mathbf{E}_m^\dagger = \mathbf{T}_h \mathbf{E}_m \mathbf{T}_h^T = \begin{bmatrix} -M + K & N \\ N & M + K \end{bmatrix}. \quad (18)$$

\mathbf{E}_m^\dagger , which is identical to the tensor examined in Waterman and Lilly (2015), has eigenvalues given by Eq. (16) and is thus positive semidefinite and describes an ellipse. This ellipse, formally the intersection between a horizontal plane and the hyperboloid described by \mathbf{E}_m , has semimajor and semiminor axis lengths given by the square root of the largest and smallest eigenvalue, respectively. The eddy anisotropy γ_m describes the eccentricity of the ellipse and \sqrt{K} determines its size. The eigenvector associated with the largest eigenvalue is

directed along the semimajor axis, and its angle ϕ_m with respect to the zonal,

$$\tan(2\phi_m) = -\frac{N}{M}, \quad (19)$$

defines direction. The Reynolds stress decomposition, Eq. (7a), readily follows by combining Eqs. (11), (17), and (19).

The horizontal ellipse, Eq. (18), and its associated eigenvectors and angle ϕ_m , is shown in Fig. 1a. The orientation of the ellipse with respect to the mean flow shear determines the sign of the horizontal cross stream momentum flux divergence and the direction of energy exchanges between the mean flow and the eddies. In the idealized case of a sheared zonal mean flow as depicted in Fig. 1b, the mean flow gains energy when the ellipse leans

with the shear ($\partial N/\partial y < 0$) and losses energy when the ellipse leans into the shear ($\partial N/\partial y > 0$), resembling the eddy–mean flow interaction implied by the “banana-shaped” eddy presented in [Wardle and Marshall \(2000\)](#).

c. Eddy form stress ellipse

Complimentary to \mathbf{E}_m , which clarifies the geometric parameters involved in decomposition (7a), the eddy form stress tensor \mathbf{E}_b provides insight into the geometric parameters in decomposition (7b). The symmetric eddy form stress tensor given by Eq. (15) has eigenvalues K and

$$\Lambda_{\pm} = \frac{L}{2}(1 \pm \gamma_t), \quad (20)$$

where

$$\gamma_t = \frac{\Lambda_+ - \Lambda_-}{\Lambda_+ + \Lambda_-} = \sqrt{\cos^2(2\lambda^*) + \sin^2(2\lambda^*)\gamma_b^2}, \quad (21)$$

and

$$\gamma_b = \frac{\mathcal{N}_0}{2|f_0|} \sqrt{\frac{R^2 + S^2}{KP}}. \quad (22)$$

The parameter γ_b constitutes an energetic bound on eddy form stress magnitude and is equivalent to a characteristic measure of the anisotropy of the eddy buoyancy flux. [Marshall et al. \(2012\)](#) show that γ_b is bounded between zero and unity, which implies that $0 \leq \gamma_t \leq 1$ as well. Hence Eq. (15) is positive semidefinite and describes an ellipsoid, the three-dimensional generalization of the ellipse. As the case for \mathbf{E}_m , the lengths of the principal axes of the ellipsoid are given by the square root of the eigenvalues. The horizontal orientation of the ellipsoid major axis, equivalent to the orientation of the eigenvector associated with the largest eigenvalue Λ_+ is given by the angle ϕ_e ,

$$\cos(\phi_e) = \mp \frac{S}{\sqrt{R^2 + S^2}}, \quad \sin(\phi_e) = \pm \frac{R}{\sqrt{R^2 + S^2}}, \quad (23)$$

which is defined with respect to the zonal direction. Since the horizontal orientation of the eddy buoyancy flux vector is defined by

$$\cos(\phi_b) = \frac{R}{\sqrt{R^2 + S^2}}, \quad \sin(\phi_b) = \frac{S}{\sqrt{R^2 + S^2}}, \quad (24)$$

it is seen that

$$\phi_e = \phi_b \pm \pi/2, \quad (25)$$

that is, the major axis of the ellipsoid leads/lags the eddy buoyancy flux vector with $\pi/2$ in the horizontal.

It is covariances between b' and \mathbf{u}'_g in \mathbf{E}_b that occupy the off-diagonal and hence suggest that a vertical section of the ellipsoid may allow for a more compact representation of the relevant eddy form stress geometry. Therefore, let \mathbf{T}_v denote the transformation matrix which consists of the two basis vectors in \mathbb{R}^3 that span the vertical plane along the major axis of the ellipsoid. Transforming \mathbf{E}_b using \mathbf{T}_v results in

$$\mathbf{E}_b^\dagger = \mathbf{T}_v \mathbf{E}_b \mathbf{T}_v^T = \begin{bmatrix} K & \frac{1}{2}\sqrt{R^2 + S^2} \\ \frac{1}{2}\sqrt{R^2 + S^2} & P^* \end{bmatrix}, \quad (26)$$

which describes the vertical ellipse at the intersection between the ellipsoid and the vertical plane aligned with its major axis. The tensor \mathbf{E}_b^\dagger has eigenvalues given by Eq. (20), which implies that the ellipse has eccentricity γ_t and size proportional to \sqrt{L} , and its horizontal orientation, described by Eq. (23), is perpendicular to the horizontal eddy buoyancy flux. The vertical orientation of the ellipse is defined by the angle between its major axis eigenvector and the horizontal plane ϕ_t , with $0 \leq \phi_t \leq \pi/2$ when the eigenvector is defined with a positive vertical component. Through the use of trigonometric identities, one finds that

$$\tan(2\phi_t) = \pm \frac{\sqrt{R^2 + S^2}}{K - P^*} = \pm \gamma_b \tan(2\lambda^*), \quad (27)$$

where it is understood that the sign varies in accord with the sign in the expression for the horizontal orientation, Eq. (23). In combination with Eq. (21), the relation for the vertical tilt provides an alternative expression for the ellipse eccentricity,

$$\gamma_t = \frac{\cos(2\lambda^*)}{\cos(2\phi_t)}. \quad (28)$$

A visualization of the vertical ellipse described by \mathbf{E}_b^\dagger is provided in [Fig. 1c](#), as well as the eigenvectors and the three angles ϕ_b , ϕ_e , and ϕ_t .

By combining Eqs. (11), (22), and (24), it is possible to arrive at the decomposition for R and S given by Eq. (7b). Alternatively, one may write this decomposition in terms of the vertical ellipse geometry via Eqs. (27) and (28),

$$\mathbf{R} = \gamma_t L \sin(2\phi_t) \mathbf{r}_b, \quad (29)$$

where $\mathbf{r}_b = [\pm \sin(\phi_e), \mp \cos(\phi_e)] = [\cos(\phi_b), \sin(\phi_b)]$. Hence the vertical ellipse described by \mathbf{E}_b^\dagger , together with the horizontal orientation of the eddy buoyancy flux, Eq. (24), provides an interpretation of the geometry involved in decomposition (7b).

Equation (26) is the main result of the present section and shows that eddy form stress is subject to a similar geometric interpretation as eddy Reynolds stress via an ellipse. A key property of the vertical ellipse is that its horizontal orientation ϕ_e is governed by the orientation of \mathbf{R} via Eq. (25), which implies that the ellipse may be used to diagnose the direction of vertical transfer of horizontal momentum in baroclinic mean flow. This follows from the dynamical equivalence between horizontal eddy buoyancy flux and eddy form stress τ_i via

$$\mathbf{R} = \frac{f_0}{\mathcal{N}_0^2} \overline{b' \mathbf{u}_g'} = -\frac{1}{\rho_0} \mathbf{k} \times \overline{\eta' \nabla_h p'} = \frac{\mathbf{k} \times \boldsymbol{\tau}_i}{\rho_0}, \quad (30)$$

where ρ_0 is the reference density, p' is the pressure deviation, and $\eta' = -b'/\mathcal{N}_0^2$ is the interface height displacement. As in Marshall et al. (2012), this use of the ellipse is depicted for an idealized vertically sheared zonal mean flow in Fig. 1d in the case where $\mathbf{R} = (0, \pm S)$, similar to the case considered in Johnson and Bryden (1989). Consistent with linear stability analysis (Eady 1949), the vertical shear weakens when the ellipse leans into the shear ($S > 0$), corresponding to the case where the energy conversion is from the mean flow to the eddies. According to decomposition (7b), the most efficient form stress at a given value for L is provided by anisotropic eddies subject to an equipartitioning of L between K and P^* , corresponding to $\lambda^* = \pi/4$. This is equivalent to a vertical ellipse with $\phi_t = \pi/4$ and $\gamma_t = \gamma_b \rightarrow 1$ via Eq. (29).

d. Marshall et al. (2012) decomposition

In Marshall et al. (2012), an eddy form stress decomposition related to Eq. (7b) is derived in terms of the eddy energy, $E = K + P$, instead of L . Defining λ to be the energy partitioning angle with respect to E ,

$$\frac{P}{E} = \sin^2(\lambda), \quad \frac{K}{E} = \cos^2(\lambda), \quad (31)$$

this decomposition follows by reformulating Eq. (7b) in terms of E and λ instead of L and λ^* ,

$$\mathbf{R} = \gamma_b \frac{|f_0|}{\mathcal{N}_0} E \sin(2\lambda) \mathbf{r}_b. \quad (32)$$

To phrase Eq. (32) in the context of the preceding subsection, consider the eddy form stress tensor

$$\mathbf{E}_w = \begin{bmatrix} K & 0 & 0 \\ 0 & K & 0 \\ -\frac{\mathcal{N}_0}{|f_0|} S & \frac{\mathcal{N}_0}{|f_0|} R & P \end{bmatrix}, \quad (33)$$

which is identical to Eq. (14), but with a weighted buoyancy variable $b' \rightarrow \mathcal{N}_0 b'/|f_0|$. By following the steps in section 2c using the symmetric part of \mathbf{E}_w instead of \mathbf{E}_b , one retrieves Eqs. (20)–(28) but now expressed in terms of E and λ instead of L and λ^* . In particular, the vertical section of \mathbf{E}_w is the vertical ellipse described by

$$\mathbf{E}_w^\dagger = \mathbf{T}_v \mathbf{E}_w \mathbf{T}_v^T = \begin{bmatrix} K & \frac{\mathcal{N}_0}{2|f_0|} \sqrt{R^2 + S^2} \\ \frac{\mathcal{N}_0}{2|f_0|} \sqrt{R^2 + S^2} & P \end{bmatrix}, \quad (34)$$

whose geometry leads to decomposition (32). Hence the difference between Eqs. (7b) and (32) is simply a rescaling of the buoyancy variable, and the vertical ellipses described by \mathbf{E}_b^\dagger and \mathbf{E}_w^\dagger orient themselves with respect to the mean flow shear in the same way via Eq. (25). Thus, section 2c also provides a clarification of the geometric parameters involved in decomposition presented in Marshall et al. (2012).

e. Eddy efficiency α

As a practical application of the geometric decomposition, the present study now follows Marshall et al. (2012) and constructs an expression for the transfer coefficient κ appropriate to the Gent and McWilliams (1990) eddy closure. The downgradient closure for the horizontal eddy buoyancy flux results in

$$\kappa = -\frac{\nabla_h \bar{b} \cdot \overline{b' \mathbf{u}_g'}}{\mathcal{M}^4} = -\frac{\mathbf{n} \cdot \overline{b' \mathbf{u}_g'}}{\mathcal{M}^2}, \quad (35)$$

where $\mathcal{M}^2 = |\nabla_h \bar{b}|$ and $\mathbf{n} = \mathcal{M}^{-2} \nabla_h \bar{b}$ is the buoyancy gradient unit vector. To remain consistent with Marshall et al. (2012), Eq. (32) is used to close for $\overline{b' \mathbf{u}_g'}$ and results in

$$\kappa = \alpha E \frac{\mathcal{N}_0}{\mathcal{M}^2}, \quad (36)$$

which is the transfer coefficient explored in Mak et al. (2017), Bachman et al. (2017), and Mak et al. (2018). The parameter α is a combination of the geometric parameters,

$$\alpha = -\gamma_b \sin(2\lambda) \text{sgn}(f_0) \mathbf{n} \cdot \mathbf{r}_b, \quad (37)$$

and is bounded by unity in magnitude, $|\alpha| \leq 1$. The boundedness of α means that it can be interpreted as a measure of how efficient baroclinic mean flow and eddies exchange energy, thus α is henceforth referred to as an *eddy efficiency*. For vertically sheared mean flow along \bar{b} contours, α is greater than zero when the ellipse leans into the shear, which can be seen by invoking the

thermal wind relation. This is consistent with down-gradient eddy buoyancy flux, $\text{sgn}(f_0)\mathbf{n} \cdot \mathbf{r}_b = -1$, in which case eddies extract energy from the mean flow. The magnitude of α is greatest when the eddy buoyancy flux is fully anisotropic, $\gamma_b = 1$, and the eddy energy E is equally partitioned between K and P , corresponding to $\lambda = \pi/4$.

The central focus of the remaining part of the paper is to explore the structure and magnitude of α in an eddy-resolving general circulation model.

3. Model setup and output postprocessing

This study uses the z-coordinate Parallel Ocean Program version 2, configured at an eddying horizontal resolution of $1/10^\circ$ on a global domain, to diagnose the eddy geometry in the Southern Ocean. A detailed account of the model setup and its comparison to the same model at 1° nominal resolution can be found in [Small et al. \(2014\)](#) and [Poulsen et al. \(2018\)](#) and references therein. This section discusses aspects of the model and its output relevant to this study only.

The model is formulated on a horizontal B grid and the vertical is discretized into 62 levels in which separation increases monotonically with depth ([Smith et al. 2010](#)). The setup includes an active sea ice model and the meteorological boundary conditions are prescribed by the CORE.v2 normal year forcing fields ([Large and Yeager 2009](#)). The forcing fields, compiled from re-analysis and observations, are updated every sixth model hour and repeat themselves after one model year. The ocean model is initiated from the World Ocean Circulation Experiment Hydrographic Climatology ([Gouretski and Koltermann 2004](#)). The model was run for 42 model years, the first 16 years at the National Center for Atmospheric Research, which are documented in [Bryan and Bachman \(2015\)](#). The model solution drifts due to the relatively short spinup, as for example seen in the horizontally averaged temperature field which is subject to a $0.2^\circ\text{C decade}^{-1}$ warming trend at 600-m depth in the Southern Ocean. Nevertheless, both the annual mean Drake Passage transport and strength of the residual overturning circulation in the Southern Ocean are stable with time ([Poulsen et al. 2018](#)).

The eddy statistics involved in the geometric framework are computed offline based on the 9 years from 34 to 42 where 3-day time-mean fields, evaluated on constant depth levels, are available. This timespan is divided into the four seasons to account for the seasonal cycle present in the meteorological forcing fields. Eddy statistics are computed within each of the four seasons and the statistics used in this study is provided by the annual

mean. All fields are horizontally coarse grained, with one grid cell on the coarse grid consisting of 10×10 grid boxes on the original fine grid. This effectively reduces the horizontal grid resolution to about $1^\circ \times 1^\circ$ and results in smoother horizontal structures.

4. Results

The present section is divided into three parts. The first part examines the structure of Southern Ocean eddy form stress and its geometric representation via the vertical ellipse outlined in [sections 2c](#) and [2d](#), the second part looks into the individual components of the form stress geometry in greater detail, and the third and last part draws together the key findings from the first two parts by presenting estimates of the eddy efficiency α . Since α is based on the form stress decomposition involving eddy energy E , the focus of the results section is on the geometric parameters related to the vertical ellipse described by \mathbf{E}_w^l , derived in [section 2d](#).

a. Eddy form stress in the Southern Ocean

[Figure 2](#) provides an overview of the spatial structure of eddy form stress \mathbf{R} in the Southern Ocean. The present analysis considers the component of \mathbf{R} projected onto $\nabla_h \bar{b}$, which is the part of the form stress relevant to mean flow along mean buoyancy contours. The vertically and meridionally averaged form stress ([Figs. 2a and 2b](#), respectively) show that it is predominantly positive, consistent with downgradient eddy buoyancy flux and downward transfer of momentum, and is elevated and vertically sustained in several locations along the path of the Antarctic Circumpolar Current (black streamlines, [Fig. 2a](#)). These regions of elevated form stress appear downstream of larger topographic obstacles, such as the Kerguelen Plateau and Drake Passage, and are in alignment with the finding presented in [Thompson and Garabato \(2014\)](#) and [Masich et al. \(2018\)](#) that eddy form stress is particularly strong in standing meanders that form in the lee of topography. Overall, the horizontal average of eddy form stress within the circumpolar current ([Fig. 2c](#)) shows that vertical stress divergence retards the mean flow above $\sim 2\text{-km}$ depth, whereas stress convergence accelerates it at greater depth.

The geometric representation of eddy form stress via the vertical ellipse, [Eq. \(34\)](#), is also shown in [Fig. 2b](#), and a number of features are readily identified. First, the ellipse size, which scales with eddy energy, is larger in regions of strong form stress and is intensified toward the surface. Second, the ellipse eccentricity γ_l is generally weak and the ellipse tilt ϕ_l deviates from $\pi/4$, suggesting an overall low buoyancy flux anisotropy γ_b and a suboptimal eddy energy partitioning. Third, the ellipse

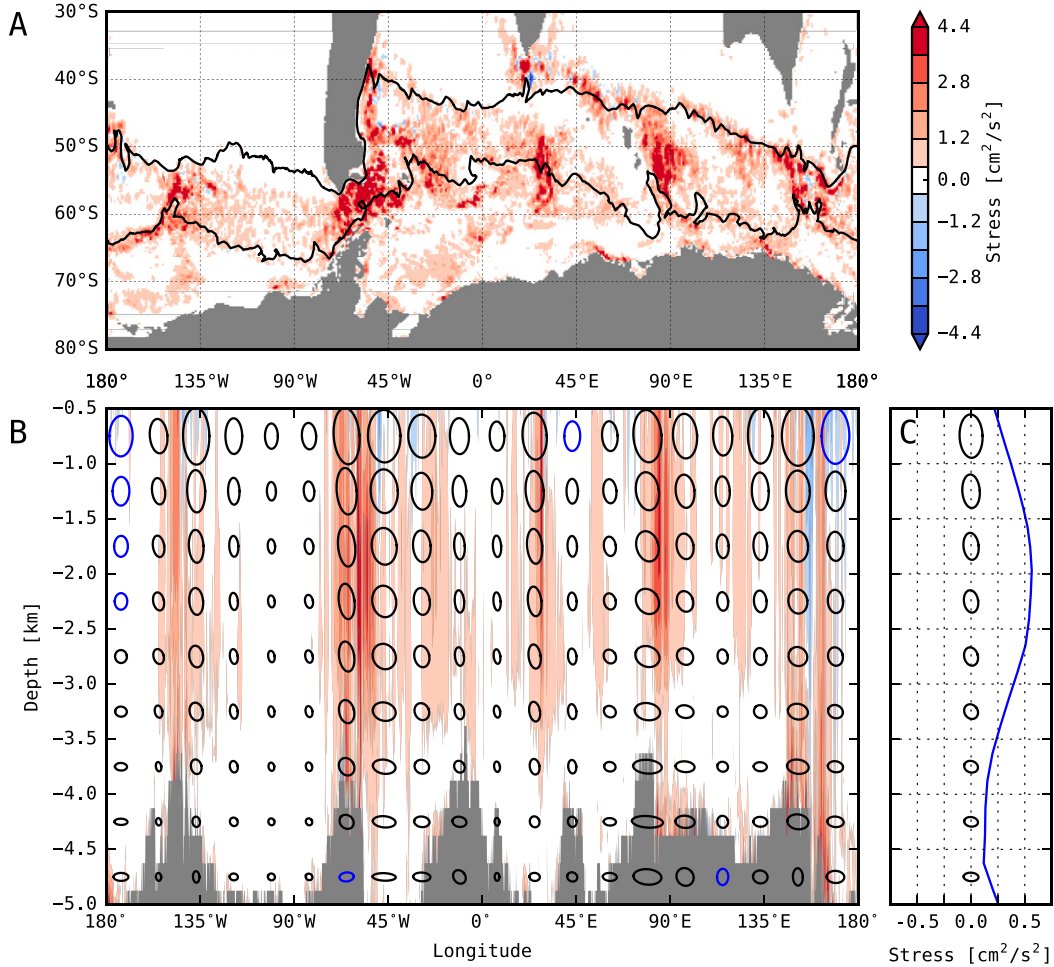


FIG. 2. (a) Vertically averaged eddy form stress below 0.5-km depth. Black lines are the 5- and 125-Sv ($1 \text{ Sv} \equiv 10^6 \text{ m}^3 \text{ s}^{-1}$) contours of the barotropic streamfunction. (b) Meridionally averaged eddy form stress within the Antarctic Circumpolar Current [defined by the black streamlines in (a)] and its geometric representation through the vertical ellipse, Eq. (34). The ellipses are based on volume averaged eddy buoyancy flux and energy calculated within 20 segments of equal longitudinal extent along the circumpolar current, with each such segment divided into nine vertical bins of approximately equal height. For visual aid, black ellipses lean into the shear and blue ellipses lean out of the shear. (c) Horizontally averaged eddy form stress and vertical ellipse within the circumpolar current. All panels are based on the vector projection of $\mathbf{R} = (R, S)$ onto $\nabla_h \bar{b}$, with a positive value indicating downgradient eddy buoyancy flux.

tilt ϕ_t tends to shift from $\pi/2$ to zero with depth, indicating that the amount of eddy potential energy exceeds eddy kinetic energy at shallow depth, and vice versa at greater depth. And last, the majority of ellipses lean into the shear (black ellipses), which is consistent with a downward momentum transfer within the baroclinically unstable circumpolar current. These ellipse characteristics are concisely summarized for the horizontally averaged circumpolar current, shown in Fig. 2c.

Provided with form stress decomposition (32), the general message from the geometric representation is that eddy energy plays a key role in setting the eddy

form stress magnitude but also that Southern Ocean eddies appear to drive an inefficient form stress given the availability of eddy energy. The low eddy efficiency is the focus of the following, which examines the eddy buoyancy flux anisotropy γ_b and eddy energy partitioning angle λ in greater detail, as these physical quantities determine the ellipse tilt ϕ_t and eccentricity γ_t via relation (21) and (27).

b. Geometric decomposition

The eddy buoyancy flux anisotropy γ_b is shown in Fig. 3a at 0.5-km depth, below the austral winter mixed layer in which \mathcal{N}_0 is ill defined. The momentum flux

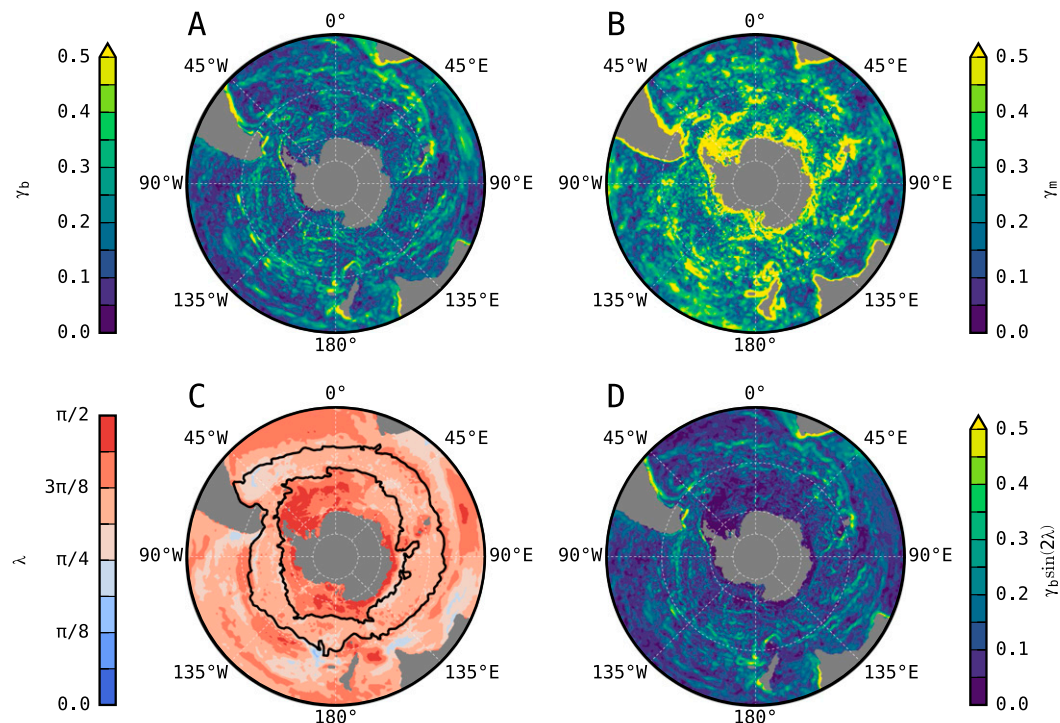


FIG. 3. Horizontal eddy flux geometry at 0.5-km depth. (a) Eddy buoyancy flux anisotropy γ_b . (b) Eddy momentum flux anisotropy γ_m . (c) Eddy energy partitioning angle λ . (d) Combination of γ_b and λ via the function $\gamma_b \sin(2\lambda)$ that appears in the expression for α , Eq. (37). The two black lines in (c) are the 5- and 125-Sv contours of the barotropic streamfunction.

anisotropy γ_m is shown in Fig. 3b for comparison. The horizontal structure of the flux anisotropies have at least three properties in common: 1) both are subject to considerable structure on the mesoscale in the interior ocean away from topographic obstacles, 2) both fields show elevated anisotropies in western boundary current regions and in proximity to larger bathymetric objects, such as the Kerguelen Plateau, and 3) neither of the fields display a clear signature of the circumpolar current system. A pronounced difference, on the other hand, is that γ_m approaches unity on the periphery of topography where γ_b does not. This property of γ_m follows from the no-normal flow boundary condition (see Marshall et al. 2012). It is also noted that the estimate of γ_m is in qualitative agreement with γ_m presented by Stewart et al. (2015), who use both satellite altimetry and high-resolution model output, indicating that the highlighted features are not model specific.

Vertical sections along the path of the Antarctic Circumpolar Current expose the same properties of the anisotropies as was shown in Fig. 3 but additionally reveals a coherent vertical structure (Figs. 4a,b). In contrast to the persistent mesoscale variations in the horizontal, γ_m shows a consistent vertical amplification with depth above rough topography and γ_b a nearly

uniform vertical structure. The former property was shown in Stewart et al. (2015) to be a result of steep gradients in f/H , H being the depth of the water column, which constrains the directionality of the eddy motion. Similar reasoning does not appear to apply in the case of γ_b , which suggests approximate isotropic eddy buoyancy fluxes in the immediate grid cells above bottom topography.

As seen from the probability distributions in Fig. 5, the momentum flux anisotropy is more widely distributed than the buoyancy flux anisotropy due to the pronounced vertical variations. The mean value of γ_m within the circumpolar current is 0.29, which is greater than the corresponding mean value of 0.15 for γ_b but lower than the global mean value of 0.42 for γ_m estimated in Stewart et al. (2015). Hence Reynolds stresses are on average more anisotropic than form stresses in the Antarctic Circumpolar Current, at least in this particular model, and the weakly anisotropic eddy buoyancy fluxes are consistent with the low ellipse eccentricity shown in Fig. 2.

The eddy energy partitioning angle λ is shown in Fig. 3c and exhibits smoother spatial variations compared to γ_b . Eddy potential energy exceeds eddy kinetic energy at this particular depth, especially in the polar

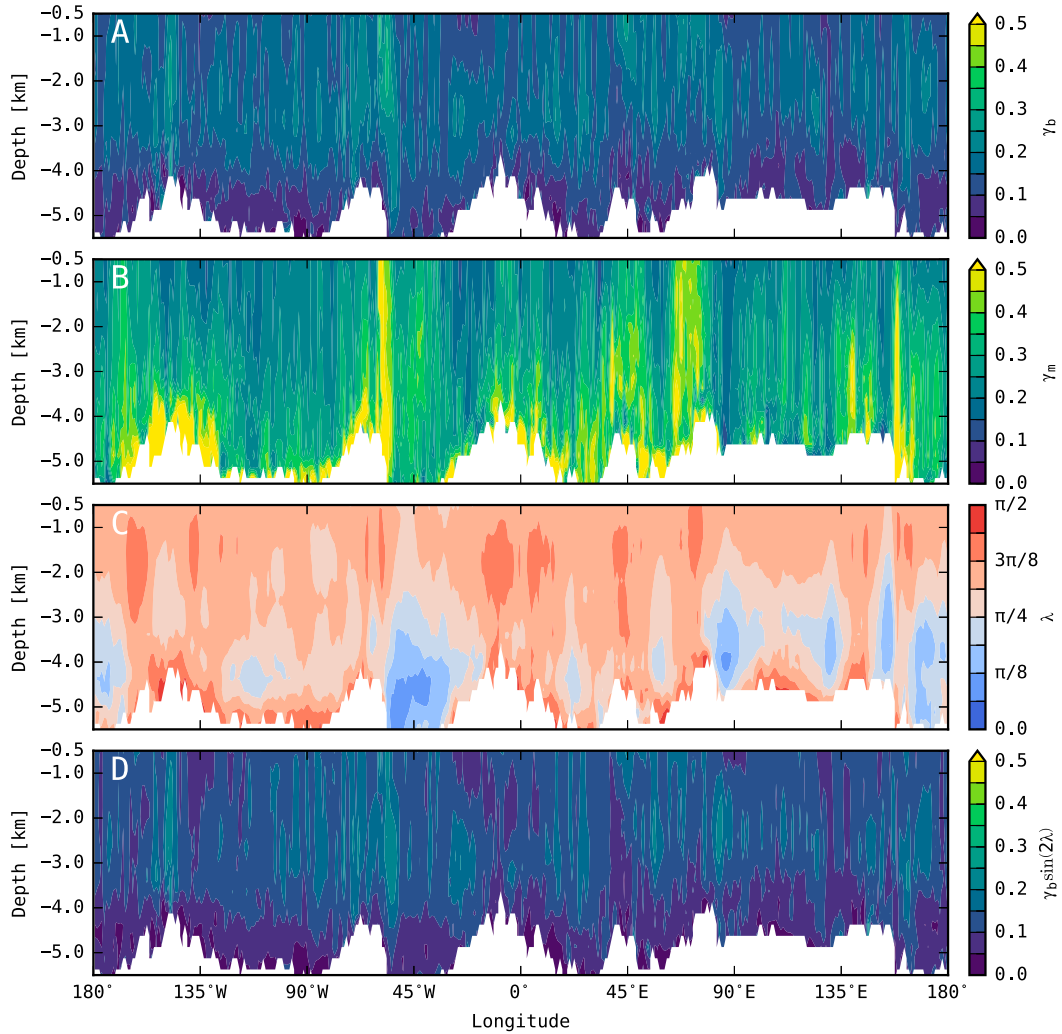


FIG. 4. Meridionally averaged sections of the horizontal eddy flux geometry within the circumpolar current envelope, shown by the two black streamlines in Fig. 2a. (a) Eddy buoyancy flux anisotropy γ_b . (b) Eddy momentum flux anisotropy γ_m . (c) Eddy energy partitioning angle λ . (d) Combination of γ_b and λ via the function $\gamma_b \sin(2\lambda)$ that appears in the expression for α , Eq. (37).

marginal seas and along the coast of Antarctica. Geostrophic scaling of the governing equations suggests $K/P \sim L_d^2/L^2$, where L_d is the baroclinic deformation radius and L is the characteristic length scale of the motion. In terms of the Eady model the most unstable wave evolves on a length scale of $3.9L_d$ (Eady 1949; Vallis 2006), corresponding to a partitioning angle $\lambda \approx 7\pi/16$, which is consistent with $K/P < 1$ as seen in the realistic eddy-resolving model. Within the current envelope the eddy energy is closer to equipartitioning ($\lambda = \pi/4$), the optimal configuration for large eddy stresses, but the associated vertical section (Fig. 4c) shows that this structure is subject to considerable variation in the vertical. This is especially visible in flat-bottomed regions where $K > P$ at greater depth, an

indication that large fluctuations in buoyancy relate to large variation in bottom topography.

c. Eddy efficiency α

Finally the focus is turned toward the eddy efficiency, Eq. (37), which takes the orientation of the eddy buoyancy flux \mathbf{r}_b with respect to the mean buoyancy gradient \mathbf{n} into account. First discussing the idealized case where the eddy buoyancy flux is directed downgradient, $\text{sgn}(f_0)\mathbf{n} \cdot \mathbf{r}_b = -1$, the expression for α reduces to

$$\alpha = \alpha_{\parallel} = \gamma_b \sin(2\lambda), \quad (38)$$

which provides an upper bound on the magnitude of the eddy efficiency, $|\alpha| \leq |\alpha_{\parallel}| \leq 1$. The horizontal

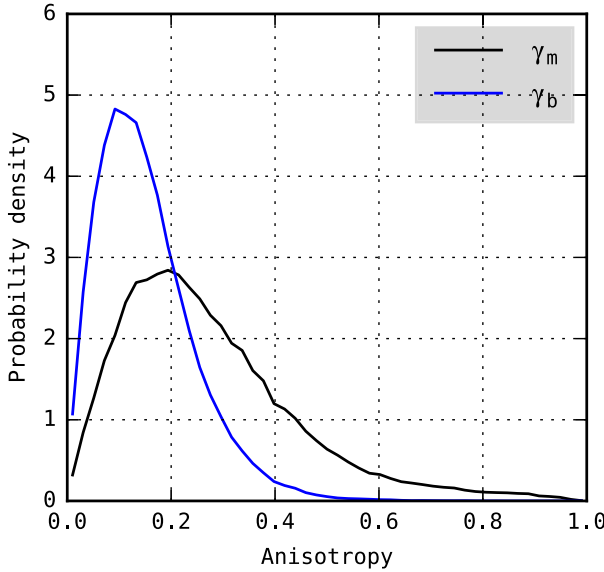


FIG. 5. Normalized probability density functions for the momentum and buoyancy flux anisotropies, γ_m and γ_b , within the current envelope defined by the streamlines in Fig. 2a and below 0.5-km depth.

distribution of α_{\parallel} is shown in Fig. 3d and reveals that it inherits its structure mostly from γ_b , despite the spatial variations in λ . Moreover, the vertical section of α_{\parallel} , shown in Fig. 4d, possesses the weak vertical structure visible in γ_b . This is promising in the context of a geometrically informed eddy closure, as it suggests that one can effectively reduce a parameterization for α_{\parallel} to the problem of representing the horizontal structure in γ_b .

Now addressing the general expression for α , Figs. 6a and 6b display the horizontal distribution of α at 0.5- and 3-km depth, respectively. At the shallow depth level the eddy efficiency is relatively weak and of mixed sign within the current envelope where it averages to 0.011. In the deep Southern Ocean, on the other hand, α is mainly positive and with a greater average of 0.077. As seen from the horizontal average within the current envelope (Fig. 7a), the efficiency monotonically increases with depth throughout the upper kilometers of the water column and peaks at about 3 km, after which it decreases again toward the ocean bottom.

Since α_{\parallel} varies weakly in the vertical, it is primarily the orientation of $\overline{b'\mathbf{u}'_g}$ with respect to $\nabla_h \bar{b}$ that governs the vertical structure in α . Figure 7b shows that the most probable orientation of the eddy buoyancy flux is perpendicular to $\nabla_h \bar{b}$ in the upper part of the Southern Ocean (solid black line), implying $\mathbf{n} \cdot \mathbf{r}_b \approx 0$, whereas the most likely orientation is downgradient at greater depth (dashed black line), $\text{sgn}(f_0) \mathbf{n} \cdot \mathbf{r}_b \approx -1$. Thus, while eddies in the Southern Ocean become increasingly energetic toward the ocean surface they also become

increasingly inefficient in interacting with the mean flow. This property, in combination with the stratification, results in the vertical structure of eddy form stress seen in Fig. 2c.

Rotational contributions to the horizontal eddy buoyancy flux, which do not influence the dynamics, may however obscure the relevant structure in α (Marshall and Shutts 1981). Based on wavenumber spectra, Griesel et al. (2009) show that the magnitude of eddy heat flux curl overwhelms the flux divergence at all relevant length scales in the Southern Ocean, and Eden (2006) finds that horizontal eddy buoyancy fluxes in the Southern Ocean tend to be more downgradient when a rotational flux contribution is removed. To quantify to what degree rotational fluxes contribute to the structure in α , a horizontal Helmholtz decomposition for the eddy buoyancy flux is considered,

$$\overline{b'\mathbf{u}'_g} = \nabla_h \chi_{\text{div}} + \mathbf{k} \times \nabla_h \chi_{\text{rot}}, \quad (39)$$

where the vector field is expressed through two scalar potentials, χ_{div} and χ_{rot} . These potentials are related to purely divergent and rotational contributions to $\overline{b'\mathbf{u}'_g}$, respectively. To estimate the divergent flux $\nabla_h \chi_{\text{div}}$, a definition for χ_{rot} is adopted from Eden et al. (2007a),

$$\chi_{\text{rot}} = |\nabla_h \bar{b}|^{-2} \overline{\mathbf{u}_g \Phi} \cdot (\mathbf{k} \times \nabla_h \bar{b}), \quad (40)$$

where $\overline{\mathbf{u}_g \Phi}$ is the flux of eddy variance, $\Phi = \overline{b'b}/2$. A detailed discussion of the assumptions which underlie Eq. (40) is found in Eden et al. (2007b). The eddy efficiency based on the estimated divergent eddy buoyancy flux is defined as

$$\alpha_{\text{div}} = -\gamma_b \sin(2\lambda) \text{sgn}(f_0) \mathbf{n} \cdot \mathbf{r}_{\text{div}}, \quad (41)$$

where $\mathbf{r}_{\text{div}} = [\cos(\phi_{b,\text{div}}), \sin(\phi_{b,\text{div}})]$ and $\phi_{b,\text{div}}$ is the horizontal angle of the divergent eddy buoyancy flux.

The effect of removing rotational eddy buoyancy fluxes mainly plays a role in the upper part of the water column. Returning to Fig. 7b, the probability distribution for the angle between the divergent flux and $\nabla_h \bar{b}$ at shallow depth is more symmetric about zero (blue solid line) and with an increased probability in the down-gradient angle interval, but the maxima at $\pm\pi/2$ persist. A minor shift in the probability density distribution is visible at greater depth (blue dashed line), but the most likely orientation of the eddy flux remains down the mean buoyancy gradient.

The implication for the eddy efficiency of removing the rotational flux contribution is therefore modest (Figs. 6c,d). Some regions of negative α are subject to a sign change at 0.5-km depth, and here α_{div} averages to 0.019. At 3-km depth, α_{div} is weaker compared to α , but

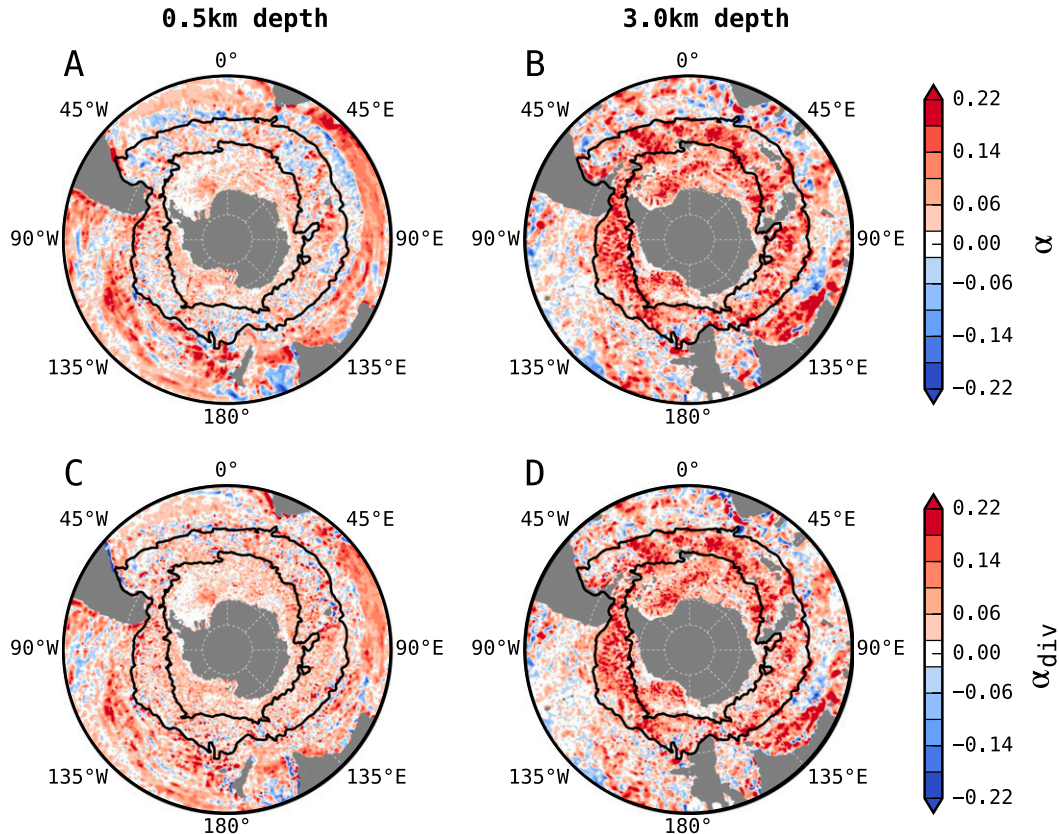


FIG. 6. (a),(b) Eddy efficiency α , Eq. (37), at 0.5- and 3.0-km depth using raw eddy buoyancy fluxes. (c),(d) Eddy efficiency α_{div} , Eq. (41), at 0.5- and 3.0-km depth using the estimated divergent eddy buoyancy flux. Black lines are the 5- and 125-Sv streamlines from the barotropic streamfunction.

the horizontal structure of the eddy efficiency does not change. The horizontally averaged profile of α_{div} (Fig. 7a) shows that it varies relatively less in the vertical, but is still subject to a pronounced maximum in the deep Southern Ocean, which appears to be a robust feature of the eddy efficiency.

To conclude the results section, probability density functions for α and α_{div} are presented in Fig. 7c. The distributions are similar and centered about positive mean values of 0.046 and 0.043 for α and α_{div} , respectively, implying that eddies extract energy from the mean flow on average, as expected, but inefficiently given that $|\alpha| \leq 1$. In summary, the low efficiency is mainly the result that horizontal eddy buoyancy fluxes are weakly anisotropic and tend to align with \bar{b} contours in the upper part of the water column where eddies are most energetic.

5. Discussion

Despite the complex horizontal structure seen in the eddy anisotropy γ_b , the probability density function in

Fig. 5 shows that horizontal eddy buoyancy fluxes in the Antarctic Circumpolar Current mainly occupy a weakly anisotropic regime, with a volume-averaged γ_b of 0.15. A similar value for the anisotropy was also estimated in Marshall et al. (2012), but for a three-layer quasigeostrophic model of a wind-driven gyre. According to Fig. 3, the anisotropy of eddy buoyancy fluxes is typically increased in those regions where topography constrains the mean flow, such as along continental boundaries and in proximity to larger submerged obstacles. Further evidence for this behavior is provided by the idealized channel model experiments presented in Youngs et al. (2017), who show that both γ_m and γ_b are higher in regions where mean flow navigates submerged topography. Of particular interest, the analysis presented here suggests that γ_b varies weakly in the vertical (Fig. 4a), which suggests that parameterization of its horizontal structure may prove adequate for use in general circulation models.

The deformation-based eddy parameterization by Anstey and Zanna (2017) suggests that eddy momentum flux anisotropy γ_m is a function of the normal and shear

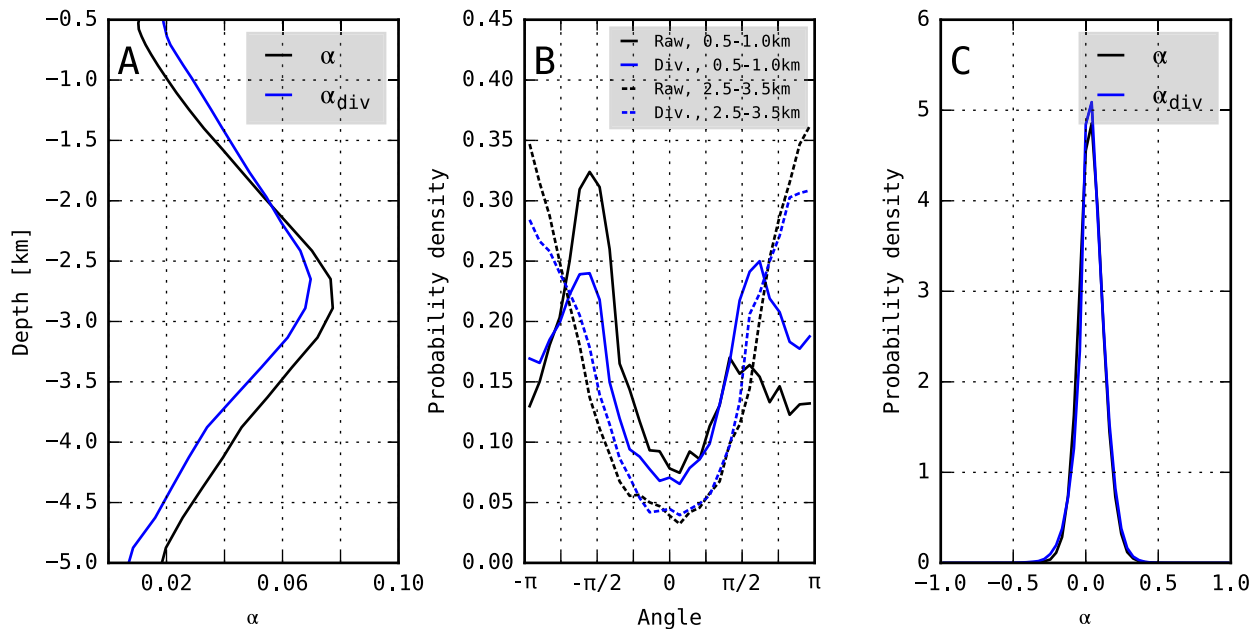


FIG. 7. (a) Horizontally averaged profiles of α and α_{div} . (b) Normalized probability density functions for the angle between $\nabla_h \bar{b}$ and the horizontal eddy buoyancy flux vector in the depth intervals 0.5–1.0 km (solid lines) and 2.5–3.5 km (dashed lines) using the raw (black) and divergent (blue) eddy buoyancy flux. A positive angle means that $\bar{b}'\bar{u}'$ leads $\nabla_h \bar{b}$. (c) Normalized probability density functions for α and α_{div} . All panels consider the part of the Southern Ocean within the circumpolar current envelope shown by the black streamlines in Fig. 2a.

strains in the large-scale flow. A related result is established by Lilly (2018), who derives a prognostic equation for the aspect ratio of a fluid ellipse in terms of the strain magnitude by the background flow. Youngs et al. (2017) finds that the greatest horizontal shear takes place when flow is topographically constrained, and hence a deformation-based view is a possible way to rationalize the regions of elevated γ_m in proximity to topography shown in Fig. 3b. Given the identified commonalities between γ_m and γ_b , it is here anticipated that a similar relationship exists for eddy buoyancy fluxes, which one may exploit to form a parameterization for γ_b .

In contrast to γ_b , the eddy efficiency α is subject to a pronounced vertical structure within the Antarctic Circumpolar Current. Here, $\alpha \approx 0.01$ at 500-m depth but is almost an order of magnitude larger at ~ 3 -km depth (Figs. 6 and 7). The higher eddy efficiency at depth is a consequence of a change in horizontal eddy buoyancy flux orientation with respect to the large-scale buoyancy gradient. Specifically, eddy buoyancy fluxes mainly align with \bar{b} contours in the upper part of the circumpolar current whereas the fluxes are predominantly down the mean buoyancy gradient in the deep Southern Ocean. Removing dynamically inert rotational fluxes reduces the variation of α with depth yet substantial vertical structure remains. The vertical variation in eddy efficiency is similar to that of eddy form stress (Fig. 2c), both displaying a pronounced peak at middepth, in contrast

to eddy energy which is most abundant at the surface. This suggests that the vertical structure in α plays an important role in shaping the vertical stress divergence and hence the eddy forcing of the mean flow.

Thus, in the context of a future parameterization for α , an outstanding challenge is to understand what sets the horizontal orientation of the eddy buoyancy flux ϕ_b . The common assumption is that the horizontal divergent eddy buoyancy flux is directed down the large-scale gradient and is related to baroclinic instability (Marshall and Shutts 1981). This relationship has been intensively studied in the past (e.g., Roberts and Marshall 2000; Eden 2006; Eden et al. 2007a,b; Griesel et al. 2009). Taken together, these works show that the down-gradient assumption may provide accurate divergent eddy flux estimates regionally but cannot be expected to hold globally. Notably, Eden et al. (2007b) demonstrate that a substantial component of the divergent eddy buoyancy flux is perpendicular to $\nabla_h \bar{b}$ in a model of the North Atlantic Current region, similar to the finding in the present study. In the quasigeostrophic mean buoyancy budget, the along-contour part of the eddy buoyancy flux can be interpreted as a horizontal eddy-induced advection of mean buoyancy, which may be as large as the mean flow advection in certain regions (Eden et al. 2007b). Hence, divergence of the along-contour eddy flux component affects the mean buoyancy budget, with implications for the stratification

and large-scale circulation, but is commonly not accounted for in ocean models without explicit eddy fluxes.

Recent implementations of the geometrically informed eddy transfer coefficient, Eq. (1), in idealized channel models have treated α as a constant. The zonally averaged model study by Mak et al. (2017) demonstrates that eddy saturation is a robust feature independent of the numerical value of α , whereas the zonal transport is inversely proportional to the eddy efficiency. In Mak et al. (2018), using a primitive equation numerical model together with a parameterization of the vertically integrated eddy energy, $\alpha = 0.04$ is deemed appropriate as it results in a channel transport for present day wind stress magnitude which matches that of an identical simulation at eddy-permitting grid resolution. This value is in agreement with the estimated average of $\alpha_{\text{div}} = 0.043$, appropriate to the Antarctic Circumpolar Current, estimated in the present study (Fig. 7). Bachman et al. (2017), on the other hand, suggests $\alpha = 0.2$ for fully developed turbulence in a channel model of the nonlinear Eady problem, and Marshall et al. (2012) show that $\alpha = 0.62$ for the most unstable mode in the linear Eady model. The eddy efficiency thus appears to decrease with increasing model complexity, such as the presence of β effects, but a complete account of this behavior remains an open question.

A natural extension to the analysis of the present study is to determine whether the eddy efficiency is a function solely of the fluid properties and imposed boundary conditions, or whether external forcing plays a role as well. This is relevant as it may have implications for modeling eddy saturation in complex numerical models, provided the inverse relationship between circumpolar transport and α (Mak et al. 2017; Marshall et al. 2017). Future work aims to quantify the sensitivity of eddy form stress, eddy energy, and eddy efficiency to changes in zonal wind stress in the high-resolution model.

Finally it is worthwhile to consider the robustness of the presented results to the numerical model's grid resolution. The model used in the present study is considered eddy resolving in the sense that the $1/10^\circ$ horizontal grid marginally resolves the first baroclinic Rossby radius of deformation; at 60°S , the deformation radius is approximately 10 km (Chelton et al. 1998) whereas the effective grid resolution is ~ 5 km. However, one may call into question whether the reported vertical structure in γ_b and α is sensitive to the model's ability to resolve the baroclinic modal structure associated with the resolved horizontal motions. Stewart et al. (2017) show that this ability depends on the number of vertical levels and their positioning, and estimate that it requires at least 50 vertical levels to resolve the first baroclinic modal structure and additionally 25 levels for

each subsequent mode. With 62 vertical levels, the model used in the present study presumably resolves the first baroclinic modal structure well, but cannot be expected to adequately resolve higher-order modes in those regions where the horizontal grid resolution permits such dynamics, for example, on shallow plateaus. The Antarctic Circumpolar Current is commonly assumed to be dominated by the first baroclinic mode, and hence it is not expected that resolving higher-order modes will change the vertical structure in γ_b and α significantly. A sensitivity test of eddy geometry to vertical model resolution is considered additional future work.

6. Summary

This study has exploited the geometric properties of the Eliassen–Palm flux tensor to reformulate eddy form stress in terms of eddy energy and a set of bounded geometric parameters related to the anisotropy, energy partitioning, and orientation of horizontal eddy buoyancy fluxes. A primary goal of the present study has been to show that the eddy form stress geometry describes an ellipse in the vertical plane which is able to serve as a diagnostic tool to determine vertical momentum transfer and exchanges of energy between mean flow and eddies. A particular focus has been the eddy efficiency α , a combination of the geometric ellipse parameters, bounded by unity in magnitude. The eddy efficiency appears in the eddy transfer coefficient appropriate to the Gent–McWilliams closure for mesoscale eddies when the geometric decomposition is used to close for the eddy buoyancy flux. Provided that it is possible to parameterize α and the eddy energy, this geometrically informed transfer coefficient can be used to close for eddy fluxes in coarse resolution ocean models in an energetically consistent way. The present study has taken initial steps toward the parameterization of α .

The geometry of Southern Ocean eddy form stress has been diagnosed in a $1/10^\circ$ eddy-resolving general circulation model and the following aspects of the eddy efficiency has been identified:

- The eddy efficiency α averages to a low but positive value of 0.043 within the Antarctic Circumpolar Current. Provided the theoretical bound on α , $|\alpha| \leq 1$, this implies that eddies extract energy from the mean flow inefficiently.
- The overall low eddy efficiency is mainly the result of weakly anisotropic eddy buoyancy fluxes. The eddy efficiency is also subject to a vertical structure with a pronounced maximum at ~ 3 -km depth, which is the result that eddy fluxes are directed most down the mean buoyancy gradient in the deep ocean.

- The vertical structure in α compensates the surface-intensified eddy energy and results in eddy form stress that is greatest at middepth. This has implication for the vertical stress divergence and hence eddy forcing of the Antarctic Circumpolar Current.

Acknowledgments. The research leading to these results has received funding from the European Research Council under the European Community's Seventh Framework Programme (FP7/2007-2013)/ERC grant agreement 610055 as part of the ice2ice project. JRM and DPM acknowledge support from the U.K. Natural Environment Research Council, NE/R000999/1. The authors gratefully acknowledge the Gauss Centre for Supercomputing (GCS) for providing computing time through the John von Neumann Institute for Computing (NIC) on the GCS share of the supercomputer JUQUEEN at Jülich Supercomputing Centre (JSC). The authors are also grateful for computing resources provided by the Danish Center for Climate Computing, a facility build with support of the Danish e-Infrastructure Corporation and the Niels Bohr Institute, as well as for Alison Baker (NCAR) for her help setting up CESM on JUQUEEN, and ERDA developers and maintainers Jonas Bardino and Klaus Birkelund Jensen for providing the computational infrastructure to analyze the model output. The model output supporting this publication is archived at www.erd.dk, and access can be obtained upon request to the corresponding author. MBP and MJ would also like to thank Carsten Eden for constructive discussions. All authors are grateful for the critique received by two anonymous reviewers, which led to an improved manuscript.

REFERENCES

- Anstey, J. A., and L. Zanna, 2017: A deformation-based parameterization of ocean mesoscale eddy Reynolds stresses. *Ocean Modell.*, **112**, 99–111, <https://doi.org/10.1016/j.ocemod.2017.02.004>.
- Bachman, S. D., D. P. Marshall, J. R. Maddison, and J. Mak, 2017: Evaluation of scalar eddy transport coefficient based on geometric constraints. *Ocean Modell.*, **109**, 44–54, <https://doi.org/10.1016/j.ocemod.2016.12.004>.
- Barthel, A., A. M. Hogg, S. Waterman, and S. Keating, 2017: Jet-topography interactions affect energy pathways to the deep southern ocean. *J. Phys. Oceanogr.*, **47**, 1799–1816, <https://doi.org/10.1175/JPO-D-16-0220.1>.
- Bischoff, T., and A. F. Thompson, 2014: Configuration of a southern ocean storm track. *J. Phys. Oceanogr.*, **44**, 3072–3078, <https://doi.org/10.1175/JPO-D-14-0062.1>.
- Böning, C. W., A. Disper, M. Visbeck, S. R. Rintoul, and F. U. Schwarzkopf, 2008: The response of the Antarctic circumpolar current to recent climate change. *Nat. Geosci.*, **1**, 864–869, <https://doi.org/10.1038/ngeo362>.
- Bryan, F. O., and S. Bachman, 2015: Isohaline salinity budget of the North Atlantic salinity maximum. *J. Phys. Oceanogr.*, **45**, 724–736, <https://doi.org/10.1175/JPO-D-14-0172.1>.
- Chelton, D. B., R. A. DeSzoeke, M. G. Schlax, K. E. Naggar, and N. Siwertz, 1998: Geographical variability of the first baroclinic Rossby radius of deformation. *J. Phys. Oceanogr.*, **28**, 433–460, [https://doi.org/10.1175/1520-0485\(1998\)028<0433:GVOTFB>2.0.CO;2](https://doi.org/10.1175/1520-0485(1998)028<0433:GVOTFB>2.0.CO;2).
- Danabasoglu, G., J. C. McWilliams, and P. R. Gent, 1994: The role of mesoscale tracer transports in the global ocean circulation. *Science*, **264**, 1123–1126, <https://doi.org/10.1126/science.264.5162.1123>.
- Eady, E. T., 1949: Long waves and cyclone waves. *Tellus*, **1**, 33–52, <https://doi.org/10.3402/tellusa.v1i3.8507>.
- Eden, C., 2006: Thickness diffusivity in the southern ocean. *Geophys. Res. Lett.*, **33**, L11606, <https://doi.org/10.1029/2006GL026157>.
- , and R. J. Greatbatch, 2008: Towards a mesoscale eddy closure. *Ocean Modell.*, **20**, 223–239, <https://doi.org/10.1016/j.ocemod.2007.09.002>.
- , —, and D. Olbers, 2007a: Interpreting eddy fluxes. *J. Phys. Oceanogr.*, **37**, 1282–1296, <https://doi.org/10.1175/JPO3050.1>.
- , —, and J. Willebrand, 2007b: A diagnosis of thickness fluxes in an eddy-resolving model. *J. Phys. Oceanogr.*, **37**, 727–742, <https://doi.org/10.1175/JPO2987.1>.
- , M. Jochum, and G. Danabasoglu, 2009: Effects of different closures for thickness diffusivity. *Ocean Modell.*, **26**, 47–59, <https://doi.org/10.1016/j.ocemod.2008.08.004>.
- Farneti, R., and Coauthors, 2015: An assessment of Antarctic Circumpolar Current and Southern Ocean meridional overturning circulation during 1958–2007 in a suite of interannual CORE-II simulations. *Ocean Modell.*, **93**, 84–120, <https://doi.org/10.1016/j.ocemod.2015.07.009>.
- Ferreira, D., J. Marshall, and P. Heimbach, 2005: Estimating eddy stresses by fitting dynamics to observations using a residual-mean ocean circulation model and its adjoint. *J. Phys. Oceanogr.*, **35**, 1891–1910, <https://doi.org/10.1175/JPO2785.1>.
- Frenger, I., M. Münnich, N. Gruber, and R. Knutti, 2015: Southern Ocean eddy phenomenology. *J. Geophys. Res. Oceans*, **120**, 7413–7449, <https://doi.org/10.1002/2015JC011047>.
- Gent, P. R., and J. C. McWilliams, 1990: Isopycnal mixing in ocean circulation models. *J. Phys. Oceanogr.*, **20**, 150–155, [https://doi.org/10.1175/1520-0485\(1990\)020<0150:IMIOC>2.0.CO;2](https://doi.org/10.1175/1520-0485(1990)020<0150:IMIOC>2.0.CO;2).
- Gouretski, V. V., and K. P. Koltermann, 2004: WOCE global hydrographic climatology: A technical report. Bundesamt für Seeschifffahrt und Hydrographie 35, 9 pp.
- Griesel, A., S. T. Gille, J. Sprintall, J. L. McClean, and M. E. Maltrud, 2009: Assessing eddy heat flux and its parameterization: A wavenumber perspective from a $1/10^\circ$ ocean simulation. *Ocean Modell.*, **29**, 248–260, <https://doi.org/10.1016/j.ocemod.2009.05.004>.
- Griffies, S. M., 1998: The Gent–McWilliams skew flux. *J. Phys. Oceanogr.*, **28**, 831–841, [https://doi.org/10.1175/1520-0485\(1998\)028<0831:TGMSF>2.0.CO;2](https://doi.org/10.1175/1520-0485(1998)028<0831:TGMSF>2.0.CO;2).
- Hallberg, R., and A. Gnanadesikan, 2001: An exploration of the role of transient eddies in determining the transport of a zonally reentrant channel. *J. Phys. Oceanogr.*, **31**, 3312–3330, [https://doi.org/10.1175/1520-0485\(2001\)031<3312:AEOTRO>2.0.CO;2](https://doi.org/10.1175/1520-0485(2001)031<3312:AEOTRO>2.0.CO;2).
- , and —, 2006: The role of eddies in determining the structure and response of the wind-driven southern hemisphere overturning: Results from the Modeling Eddies in the Southern Ocean (MESO) project. *J. Phys. Oceanogr.*, **36**, 2232–2252, <https://doi.org/10.1175/JPO2980.1>.
- Hoskins, B. J., I. N. James, and G. H. White, 1983: The shape, propagation and mean flow interaction of large-scale weather systems. *J. Atmos. Sci.*, **40**, 1595–1612, [https://doi.org/10.1175/1520-0469\(1983\)040<1595:TSPAMF>2.0.CO;2](https://doi.org/10.1175/1520-0469(1983)040<1595:TSPAMF>2.0.CO;2).

- Ivchenko, V. O., K. J. Richards, and D. P. Stevens, 1996: The dynamics of the Antarctic Circumpolar Current. *J. Phys. Oceanogr.*, **26**, 753–774, [https://doi.org/10.1175/1520-0485\(1996\)026<0753:TDOTAC>2.0.CO;2](https://doi.org/10.1175/1520-0485(1996)026<0753:TDOTAC>2.0.CO;2).
- Jochum, M., and C. Eden, 2015: The connection between Southern Ocean winds, Atlantic meridional overturning circulation, and Indo-Pacific upwelling. *J. Climate*, **28**, 9250–9256, <https://doi.org/10.1175/JCLI-D-15-0263.1>.
- Johnson, G. C., and L. H. Bryden, 1989: On the size of the Antarctic Circumpolar Current. *Deep-Sea Res.*, **36**, 39–55, [https://doi.org/10.1016/0198-0149\(89\)90017-4](https://doi.org/10.1016/0198-0149(89)90017-4).
- Large, W. G., and S. G. Yeager, 2009: The global climatology of an interannually varying air-sea flux data set. *Climate Dyn.*, **33**, 341–364, <https://doi.org/10.1007/s00382-008-0441-3>.
- Lilly, J. M., 2018: Kinematics of a fluid ellipse in a linear flow. *Fluids*, **3**, 16, <https://doi.org/10.3390/fluids3010016>.
- Maddison, J., and D. Marshall, 2013: The Eliassen–Palm flux tensor. *J. Fluid Mech.*, **729**, 69–102, <https://doi.org/10.1017/jfm.2013.259>.
- Mak, J., D. P. Marshall, J. R. Maddison, and S. D. Bachman, 2017: Emergent eddy saturation from an energy constrained eddy parameterization. *Ocean Modell.*, **112**, 125–138, <https://doi.org/10.1016/j.ocemod.2017.02.007>.
- , J. R. Maddison, D. P. Marshall, and D. R. Munday, 2018: Implementation of a geometrically and energetically constrained mesoscale eddy parameterization in an ocean circulation model. *J. Phys. Oceanogr.*, **48**, 2363–2382, <https://doi.org/10.1175/JPO-D-18-0017.1>.
- Marshall, D. P., 1997: Subduction of water masses in an eddying ocean. *J. Mar. Res.*, **55**, 201–222, <https://doi.org/10.1357/0022240973224373>.
- , J. R. Maddison, and P. S. Berloff, 2012: A framework for parameterizing eddy potential vorticity fluxes. *J. Phys. Oceanogr.*, **42**, 539–557, <https://doi.org/10.1175/JPO-D-11-048.1>.
- , M. H. P. Ambaum, J. R. Maddison, D. R. Munday, and L. Novak, 2017: Eddy saturation and frictional control of the Antarctic Circumpolar Current. *Geophys. Res. Lett.*, **44**, 286–292, <https://doi.org/10.1002/2016GL071702>.
- Marshall, J., and G. Shutts, 1981: A note on rotational and divergent eddy fluxes. *J. Phys. Oceanogr.*, **11**, 1677–1680, [https://doi.org/10.1175/1520-0485\(1981\)011<1677:ANORAD>2.0.CO;2](https://doi.org/10.1175/1520-0485(1981)011<1677:ANORAD>2.0.CO;2).
- , and T. Radko, 2003: Residual-mean solutions for the Antarctic Circumpolar Current and its associated overturning circulation. *J. Phys. Oceanogr.*, **33**, 2341–2354, [https://doi.org/10.1175/1520-0485\(2003\)033<2341:RSFTAC>2.0.CO;2](https://doi.org/10.1175/1520-0485(2003)033<2341:RSFTAC>2.0.CO;2).
- Masich, J., T. K. Chereskin, and M. R. Mazloff, 2015: Topographic form stress in the Southern Ocean state estimate. *J. Geophys. Res. Oceans*, **120**, 7919–7933, <https://doi.org/10.1002/2015JC011143>.
- , M. R. Mazloff, and T. K. Chereskin, 2018: Interfacial form stress in the southern ocean state estimate. *J. Geophys. Res. Oceans*, **123**, 3368–3385, <https://doi.org/10.1029/2018JC013844>.
- Meredith, M. P., and A. M. Hogg, 2006: Circumpolar response of southern ocean eddy activity to a change in the southern annular mode. *Geophys. Res. Lett.*, **33**, L16608, <https://doi.org/10.1029/2006GL026499>.
- Morrison, A. K., and A. M. Hogg, 2013: On the relationship between Southern Ocean overturning and ACC transport. *J. Phys. Oceanogr.*, **43**, 140–148, <https://doi.org/10.1175/JPO-D-12-057.1>.
- Morrow, R., R. Coleman, J. Church, and D. Chelton, 1994: Surface eddy momentum flux and velocity variances in the southern ocean from Geosat altimetry. *J. Phys. Oceanogr.*, **24**, 2050–2071, [https://doi.org/10.1175/1520-0485\(1994\)024<2050:SEMAV>2.0.CO;2](https://doi.org/10.1175/1520-0485(1994)024<2050:SEMAV>2.0.CO;2).
- Munday, D. R., H. L. Johnson, and D. P. Marshall, 2013: Eddy saturation of equilibrated circumpolar currents. *J. Phys. Oceanogr.*, **43**, 507–532, <https://doi.org/10.1175/JPO-D-12-095.1>.
- Munk, W. H., and E. Palmén, 1951: Note on the dynamics of the Antarctic Circumpolar Current. *Tellus*, **3**, 53–55, <https://doi.org/10.3402/tellusa.v3i1.8609>.
- Olbers, D., 1998: Comments on “On the obscurantist physics of ‘form drag’ in theorizing about the circumpolar current.” *J. Phys. Oceanogr.*, **28**, 1647–1654, [https://doi.org/10.1175/1520-0485\(1998\)028<1647:COOTOP>2.0.CO;2](https://doi.org/10.1175/1520-0485(1998)028<1647:COOTOP>2.0.CO;2).
- Poulsen, M. B., M. Jochum, and R. Nuterman, 2018: Parameterized and resolved southern ocean eddy compensation. *Ocean Modell.*, **124**, 1–15, <https://doi.org/10.1016/j.ocemod.2018.01.008>.
- Riley, K. F., M. P. Hobson, and S. J. Bence, 2006: *Mathematical Methods for Physics and Engineering*. 3rd ed. Cambridge University Press, 1333 pp.
- Roberts, M. J., and D. P. Marshall, 2000: On the validity of down-gradient eddy closures in ocean models. *J. Geophys. Res.*, **105**, 28 613–28 627, <https://doi.org/10.1029/1999JC000041>.
- Roulet, G., X. Capet, and G. Maze, 2014: Global interior eddy available potential energy diagnosed from Argo floats. *Geophys. Res. Lett.*, **41**, 1651–1656, <https://doi.org/10.1002/2013GL059004>.
- Small, R. J., and Coauthors, 2014: A new synoptic scale resolving global climate simulation using the community earth system model. *J. Adv. Model. Earth Syst.*, **6**, 1065–1094, <https://doi.org/10.1002/2014MS000363>.
- Smith, R. D., and Coauthors, 2010: The Parallel Ocean Program (POP) reference manual: Ocean component of the Community Climate System Model (CCSM). Tech. Rep. LAUR-10-01853, Los Alamos National Laboratory, 141 pp., <http://www.cesm.ucar.edu/models/cesm1.0/pop2/doc/sci/POPRefManual.pdf>.
- Stewart, K. D., P. Spence, S. Waterman, J. Le Sommer, J.-M. Molines, J. M. Lilly, and M. H. England, 2015: Anisotropy of eddy variability in the global ocean. *Ocean Modell.*, **95**, 53–65, <https://doi.org/10.1016/j.ocemod.2015.09.005>.
- , A. M. Hogg, S. M. Griffies, A. P. Heerdegen, M. L. Ward, P. Spence, and M. H. England, 2017: Vertical resolution of baroclinic modes in global ocean models. *Ocean Modell.*, **113**, 50–65, <https://doi.org/10.1016/j.ocemod.2017.03.012>.
- Storch, J. V., C. Eden, I. Fast, H. Haak, D. Hernández-Decker, E. Maier-Reimer, J. Marotzke, and D. Stammer, 2012: An estimate of the Lorenz energy cycle for the world ocean based on the 1/10° STORM/NCEP simulation. *J. Phys. Oceanogr.*, **42**, 2185–2205, <https://doi.org/10.1175/JPO-D-12-079.1>.
- Straub, D. N., 1993: On the transport and angular momentum balance of channel models of the Antarctic Circumpolar Current. *J. Phys. Oceanogr.*, **23**, 776–782, [https://doi.org/10.1175/1520-0485\(1993\)023<0776:OTTAAM>2.0.CO;2](https://doi.org/10.1175/1520-0485(1993)023<0776:OTTAAM>2.0.CO;2).
- Tamarin, T., J. R. Maddison, E. Heifetz, and D. P. Marshall, 2016: Geometric interpretation of eddy Reynolds stresses in barotropic ocean jets. *J. Phys. Oceanogr.*, **46**, 2285–2307, <https://doi.org/10.1175/JPO-D-15-0139.1>.
- Tamsitt, V., and Coauthors, 2017: Spiraling pathways of the global deep waters to the surface of the southern ocean. *Nat. Commun.*, **8**, 172, <https://doi.org/10.1038/s41467-017-00197-0>.
- Thompson, A. F., and A. C. N. Garabato, 2014: Equilibration of the Antarctic Circumpolar Current by standing meanders. *J. Phys. Oceanogr.*, **44**, 1811–1828, <https://doi.org/10.1175/JPO-D-13-0163.1>.
- Vallis, G. K., 2006: *Atmospheric and Oceanic Fluid Dynamics*. 1st ed. Cambridge University Press, 745 pp.

- Viebahn, J., and C. Eden, 2010: Towards the impact of eddies on the response of the southern ocean to climate change. *Ocean Modell.*, **34**, 150–165, <https://doi.org/10.1016/j.ocemod.2010.05.005>.
- Visbeck, M., J. Marshall, T. Haine, and M. Spall, 1997: Specification of eddy transfer coefficients in coarse-resolution ocean circulation models. *J. Phys. Oceanogr.*, **27**, 381–402, [https://doi.org/10.1175/1520-0485\(1997\)027<0381:SOETCI>2.0.CO;2](https://doi.org/10.1175/1520-0485(1997)027<0381:SOETCI>2.0.CO;2).
- Wardle, R., and J. Marshall, 2000: Representation of eddies in primitive equation models by a PV flux. *J. Phys. Oceanogr.*, **30**, 2481–2503, [https://doi.org/10.1175/1520-0485\(2000\)030<2481:ROEIP>2.0.CO;2](https://doi.org/10.1175/1520-0485(2000)030<2481:ROEIP>2.0.CO;2).
- Waterman, S., and B. J. Hoskins, 2013: Eddy shape, orientation, propagation, and mean flow feedback in western boundary current jets. *J. Phys. Oceanogr.*, **43**, 1666–1690, <https://doi.org/10.1175/JPO-D-12-0152.1>.
- , and J. M. Lilly, 2015: Geometric decomposition of eddy feedbacks in barotropic systems. *J. Phys. Oceanogr.*, **45**, 1009–1024, <https://doi.org/10.1175/JPO-D-14-0177.1>.
- Wolff, J.-O., E. Maier-Reimer, and D. J. Olbers, 1991: Wind-driven flow over topography in a zonal β -plane channel: A quasi-geostrophic model of the Antarctic Circumpolar Current. *J. Phys. Oceanogr.*, **21**, 236–264, [https://doi.org/10.1175/1520-0485\(1991\)021<0236:WDFOTI>2.0.CO;2](https://doi.org/10.1175/1520-0485(1991)021<0236:WDFOTI>2.0.CO;2).
- Youngs, M. K., A. F. Thompson, A. Lazar, and K. J. Richards, 2017: ACC meanders, energy transfer, and mixed barotropic-baroclinic instability. *J. Phys. Oceanogr.*, **47**, 1291–1305, <https://doi.org/10.1175/JPO-D-16-0160.1>.